

On high stiffness of soft robots for compatibility of deformation and function

Keisuke Hagiwara, Ko Yamamoto, Yoshihisa Shibata, Mitsuo Komagata & Yoshihiko Nakamura

To cite this article: Keisuke Hagiwara, Ko Yamamoto, Yoshihisa Shibata, Mitsuo Komagata & Yoshihiko Nakamura (2022) On high stiffness of soft robots for compatibility of deformation and function, Advanced Robotics, 36:19, 995-1010, DOI: [10.1080/01691864.2022.2117574](https://doi.org/10.1080/01691864.2022.2117574)

To link to this article: <https://doi.org/10.1080/01691864.2022.2117574>



[View supplementary material](#)



Published online: 08 Sep 2022.



[Submit your article to this journal](#)



Article views: 143



[View related articles](#)



CrossMark

[View Crossmark data](#)



FULL PAPER



On high stiffness of soft robots for compatibility of deformation and function

Keisuke Hagiwara ^a, Ko Yamamoto ^a, Yoshihisa Shibata ^a, Mitsuo Komagata ^a and Yoshihiko Nakamura ^b

^aGraduate School of Information Science and Technology, The University of Tokyo, Tokyo, Japan; ^bGraduate School of Engineering, The University of Tokyo, Tokyo, Japan

ABSTRACT

This study investigates the compatibility between the soft deformation and high stiffness through the development of a soft robotic gripper for a human-scale payload. Softness is important for robotic systems that physically interact with the environments, especially for adaptive grasping or manipulation of unknown objects. Pursuing only softness would not achieve them either, and creating a certain stiffness is also an essential function in many human-scale applications. Soft robotics is unique in that it employs soft materials for the structure, and will find a lot more applications if it gains the human-scale specifications of force or the equivalent stiffness. We discuss the compatibility of the soft deformation and high stiffness based on a numerical analysis, and then present the design of a soft robotic gripper actuated by high oil-pressure, reporting its experimental validations.

ARTICLE HISTORY

Received 23 December 2021

Revised 4 June 2022

Accepted 11 August 2022

KEYWORDS

Soft robotics; high stiffness; payload capacity; robotic gripper; hydraulic actuators

1. Introduction

Softness is important for robotic systems that physically interact with the environments. Adaptive grasping or dexterous manipulation would not be achieved without softness. Pursuing only softness would not achieve them either, since a soft structure often fails to create a large force for pinching or a stiffness against the environments. We know that creating a certain stiffness is an essential function in many applications for robot manipulators. It would not overly narrow the scope of discussion to consider the human scale for specifications, since a Cobot, namely, a robot intended for direct human robot interaction [1] is growing its applications and markets. We mean by the human scale a few tens of Newton for pinching or grasping (for a few kg payload) and a few hundreds of Newton for a manipulation.

Soft robotics [2, 3] is unique in that it employs soft materials for the robot structure. Distributed deformation is achieved by actuating a structure made of soft materials, which is suitable especially for forming-type grasping due to its passive deformation. Soft robotics already has some applications in industrial robots [4], surgical robots [5], rehabilitation [6], exploration in a disaster site [7], and food manipulation [8]. Some soft robot hands are already commercially available [9]. A soft robot typically employs the air pressure to actuate its inflatable

structure made of silicone rubber, where the common specifications are 10–500 kPa of air pressure and 20–30 of Shore A hardness. While the specifications offer good softness on one hand, they seldom meet the human scale requirements on the other hand.

The soft robotics will find a lot more applications if it gains the human-scale specifications of force or the equivalent stiffness. Constructive approaches would include to (1) select appropriate fluid and materials, (2) design functional geometry of structure, and (3) control between the soft deformation and the high stiffness. Since the compressibility of air-pressure makes its positioning difficult and creates heat in high pressure, it is commonly used in relatively low-pressure lower than 0.8 MPa. An oil-pressure is another candidate of the fluid and it is used commonly at high pressure as much as 20 MPa. A problem in employing the oil-pressure for a soft robot is the oil resistance of soft material. Although silicone rubber is widely used to fabricate sophisticated 3D shape, it is not oil-resistant. The nitrile butadiene rubber (NBR) among oil-resistant rubber materials is used to exploit large power in the McKibben type oil-pressure actuator [10]. The study on the relationship between the soft deformation and the high stiffness has been still open partially because the degree-of-freedom in the geometric design of NBR is not high due to the difficulty of fabrication.

CONTACT Ko Yamamoto yamamoto.ko@ynl.t.u-tokyo.ac.jp

Supplemental data for this article can be accessed here. <https://doi.org/10.1080/01691864.2022.2117574>

In this study, we investigate the compatibility between the soft deformation and high stiffness through the development of a soft robotic gripper that is for a human-scale payload. We employ oil-pressure and use NBR as an oil-resistant material. The conditions among working fluid, pressure and its control, and composite design of materials are numerically investigated based on a simple geometry like the spherical shell structure. We then use the knowledge of conditions and apply to the design and fabrication of a soft robotic gripper. We conduct experiments using the soft robotic gripper and report on the experiments.

The rest of the paper is organized as follows. In Section 2, we discuss the compatibility of the soft deformation and the high stiffness based on the numerical finite element analysis. Then, Section 3 presents the design and fabrication of the soft robotic gripper. Section 4 and 5 show the experiments with the curvature control by visual feedback. Finally, Section 6 describes the conclusion of this paper.

2. Compatibility of soft deformation and high stiffness

2.1. Actuation types of continuously-deformed soft robot

Even soft robot hands, an example of a soft robot, there are many different types [11]. In this paper, we limit the problem to the fluidic elastomer actuator, which is a typical hydraulic soft actuator and inflates with fluid. Figure 1 shows the classification of the fluidic elastomer actuator based on actuation types, which are the ways to generate output and bending motion with asymmetric structures. This classification is summarized as follows:

- (a) Eccentricity type [12] generates a bending motion by utilizing the difference of the thickness. The advantage of this type is that the fabrication is easy whereas the disadvantage is that the bending motion is small.

- (b) Slit type [13] has a soft cylinder and a rigid cover. As shown in Figure 1(b), one side of the cover has slits. The inner soft cylinder expands at those slits, which generates a bending motion.
- (c) Bellows type [8, 14] consists of a complicated shape with multiple chambers on one side of the structure. Each chamber expands when the inner fluid is pressurized, which generates a bending motion. The advantage of this type is that a large bending motion is obtained whereas the disadvantage is that the shape is complicated, and its fabrication is difficult.
- (d) Fiber-constraint type [15, 16] constrains a soft cylinder by strings or wires. An anisotropic constraint generates a bending motion when the inner fluid is pressurized. Note that we need either dividing interior of the finger into several spaces by axial partitions or embedding an inextensible material on one side of the finger to generate a bending motion.

The resultant stiffness depends on the selection of not only the actuation type but also the inner fluid. In the next subsection, we discuss a simple thought experiment to evaluate how much stiffness is obtained.

2.2. Analysis on stiffness by pressure and property of fluid

In this paper, in order to find the conditions for achieving high stiffness in a soft robot, we focus on the fluid. Figure 2 shows a schematic illustration of the thought experiment. A spherical shell made with a soft material is sandwiched by two rigid plates, where the lower plate is fixed. We assume that inner pressure is applied to the shell or that a fluid is filled inside the shell. Then, we apply a force to the upper plate and measure the deformation of the shell in the vertical direction, which is calculated by the finite element analysis (FEA). Although this is a simple simulation, it is a model of a fluid-driven soft robot

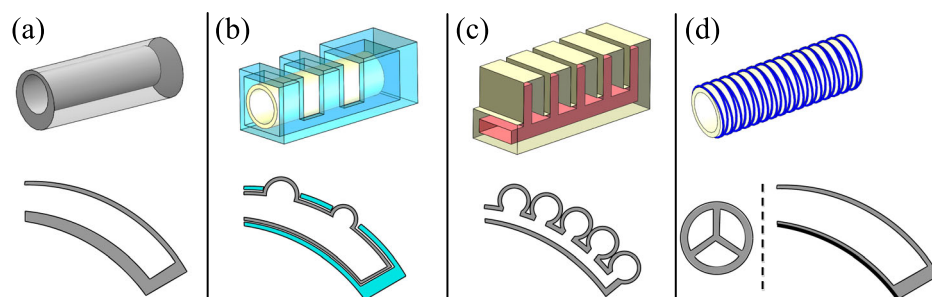


Figure 1. Classification of fluidic elastomer actuator: (a) eccentricity type, (b) slit type, (c) bellows type, and (d) fiber-constraint type.

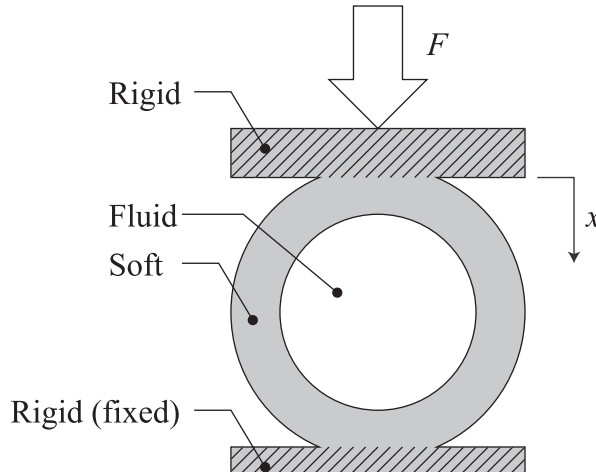


Figure 2. Schematic view of a thought experiment to evaluate stiffness of a spherical shell made with soft material and filled with a fluid inside.

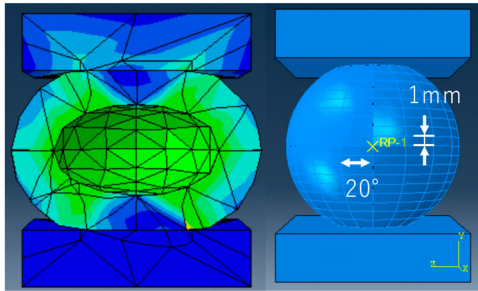


Figure 3. (Left) The cross section of the shell filled with oil when 100 N is applied. (Right) The fiber-constraint shell.

Table 1. Material properties used in FEA simulation.

Spherical shell (diameter: 20 mm, thickness: 4 mm)		
Material	Young's modulus	Poisson's ratio
NBR	5.7 MPa	0.49
Kevlar thread	31.067 GPa	0.36
Rigid plate (thickness: 5 mm)		
Material	Young's modulus	Poisson's ratio
Aluminum	69 GPa	0.3

that supports a load, and we can estimate the potential stiffness.

Figure 3 shows the state of the simulation. We used Abaqus (Simulia, Dassault Systemes, RI) for the FEA computation. We assume NBR as the material of the sphere, which is a typical oil-resistant rubber, as an example. Table 1 summarizes the setting of the material parameters. The details of the parameter setting are described in Appendix A. Figure 4 shows the relationship between the displacement x and the external force F obtained from all the simulation cases described below.

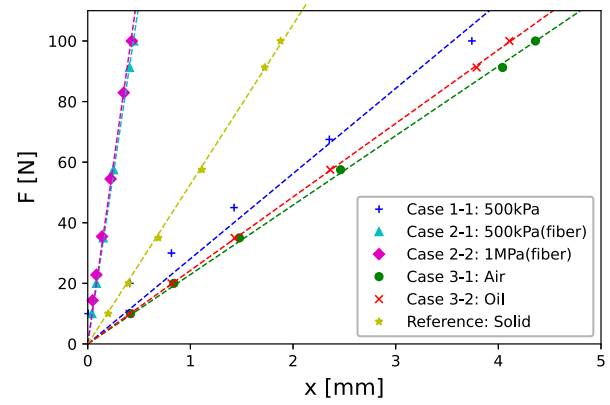


Figure 4. The FEA simulation result of external force and displacement of the spherical shell. The case of a solid sphere was prepared as a reference.

We first investigate the effect of the inner pressure which the fluid applies to the robot on the stiffness. In this simulation, we assume an ideal pressure control in which the flow rate is adjusted to achieve the desired pressure, which implies that the same simulation result is obtained for different fluids. Therefore, the shell is not filled with a fluid to simplify the simulation. If we consider the case that the shell is filled with a fluid under pressure control, we need to consider an expansion of the fluid as the increase of the inner pressure. However, this requires more complicated fluid dynamics computation. We consider that the simplified case that the shell is not filled with a fluid is sufficient to analyze the effect of the inner pressure to the macroscopic stiffness of the shell. The inner pressure did not change in this simulation because the ideal pressure control was assumed. The simulation was performed in the following two cases.

Case 1-1: 500 kPa inner pressure
Case 1-2: 1 MPa inner pressure

However, in Case 1-2 the shell expanded laterally too much and the calculation did not converge in the simulation. According to Gent et al. [17], while the spherical shell expands, the inner pressure is not increasing monotonically but has a peak then decreases. From this, in order to achieve high pressure control, we consider that it is necessary to suppress too much expansion of the shell for making the peak of the inner pressure higher and avoiding the decrease. Therefore, we expected that (d) fiber-constraint type, which suppresses the radial expansion most in Figure 1, would have the effect, and performed the simulation in the following two cases.

Case 2-1: 500 kPa inner pressure and fiber-constraint
Case 2-2: 1 MPa inner pressure and fiber-constraint

In these cases, an excessive expansion was suppressed and the calculation converged. In addition, Case 2-2 (1 MPa, indicated by the magenta line in Figure 4) was slightly more rigid than Case 2-1 (500 kPa, indicated by the cyan line). Therefore, it can be seen that high inner pressure contributes to high stiffness.

While the previous simulation assumed an ideal pressure control, it is also possible in a practical use of a soft robot that the pressure is not explicitly controlled and the resultant stiffness depends mainly on the filled fluid property. Therefore, we next focus on the property of the fluid itself and investigate how the difference between oil and air affects the stiffness when the fluid is only filled inside the shell without pressure control or fiber-constraint. In this simulation, the inner pressure was set to 0 Pa at first, then, was changed by the external force. The simulation was performed in the following two cases.

Case 3-1: filled with air (compressive fluid)

Case 3-2: filled with oil (incompressive fluid)

As shown in Figure 4, Case 3-2 (oil, indicated by the red line) is more rigid than Case 3-1 (air, indicated by the green line). This is because the oil is an incompressible fluid while the air is a compressive one.

From these comparisons, it was found that higher inner pressure contributed to higher stiffness under ideal pressure control and that the incompressible fluid contributed to higher stiffness under no pressure control. Moreover, there is a possibility that fiber-constraint affects the achievement of high inner pressure. The result of Case 2-2 shows that this structure has 0.2 mm displacement when 50 N force is applied, namely, 250 N/mm stiffness. This is comparable with the stiffness of human muscle tendon: 1 GPa, about 140–150 N/mm [2, 18]. Therefore, we consider that the stiffness of fiber-constraint material actuated by high oil pressure can achieve a human-scale heavy object supporting.

2.3. Selection of material and fabrication

From the results of the previous subsection, we select the combination of high pressure, oil and fiber-constraint type for our soft robot. However, there are multiple candidates for materials and fabrication methods. Figure 5 summarizes possible candidates of each factor and their combinations. The candidates of the oil-resistant material are as follows:

- Fluoro-rubber (FKM) is the most oil-resistant material; however, it is known that the cost is expensive.

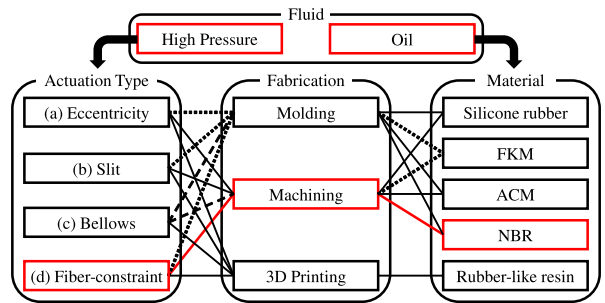


Figure 5. Relationship among fluid, actuation types, materials and fabrications. Solid lines indicate possible options, dashed lines indicate technically difficult options, and dotted lines indicate expensive options. The red lines are our choice.

- Acrylic rubber (ACM) is also oil-resistant material; however, the disadvantage is that ACM is not resistant for water and some of ester base synthetic oil.
- NBR is a standard material commonly used in an oil-hydraulic machine, as an oil seal for example.
- Rubber-like resins used in 3D printer is also a candidate of material because some of them are oil-resistant, such as TangoGray (FLX950). ¹ Although 3D printer allows us to fabricate a complicated 3D shape, the anisotropy by the printing direction and weak tensile strength ² are not suitable for the high-pressure actuation: a rubber-like resin often tear, and oil leaks out during deformation.

Therefore, we employ NBR for the main structure and rubber-like resins for the other components of soft actuators.

The fabrication method of the oil-resistant materials includes molding and machining in addition to 3D printing. Although metal molding of NBR is capable of a complicated 3D shape, the cost is very expensive. Moreover, when using metal molding, the fabricated shape is limited to one that can be extracted from the mold. Therefore, multiple mold parts tend to be required even for a simple cylindrical shape.

Another candidate of the fabrication is machining. Simple shapes of NBR are usually manufactured by machining. It is not appropriate for (c) the bellows type because the machining cannot fabricate complicated shape, but applicable for (a), (b), or (d) in Figure 1. Therefore, we select machining for fiber-constraint type.

In this section, by focusing on fluid first and finding the conditions to achieve high stiffness, we can make an appropriate selection for each design factor.

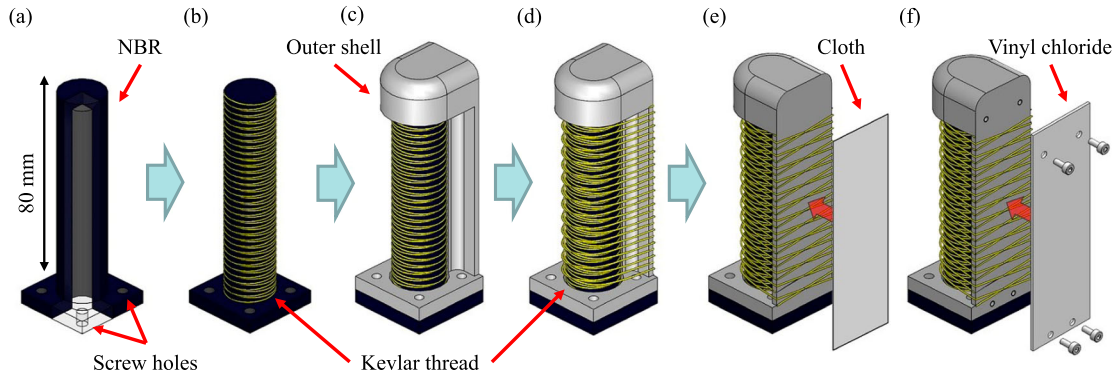


Figure 6. (a) Three-quarters cutaway diagram of NBR. Using cutting, the NBR was shaped like a cylinder attached to a square base. (b) The NBR cylinder is wrapped with Kevlar thread in a double helix. (c) The cylinder is covered with the outer shell. The outer shell is made by 3D printer, the tip and bottom are made of hard resin and the part along the NBR is made of rubber-like resin. (d) The outer shell and the cylindrical part of NBR are fixed with Kevlar thread. (e) A cloth is attached (for normal operation) or (f) vinyl chloride is screwed (for heavy objects) to the ventral side for reinforcement.

2.4. Fiber-constraint soft finger

Figure 6 shows a soft robot finger that we developed. A cylinder made with NBR is constrained by Kevlar thread and a resin outer shell, which generates a bending motion. We used NBR with Shore A hardness 70. The length, outer diameter, and thickness of the cylinder are 80, 18, and 4 mm, respectively. That is, the hardness, thickness, and diameter are almost the same as the parameters of the FEA in Section 2.

The outer shell is integrally molded, and TangoGray is used for the part bending together with NBR, hard resin VeroWhite (RGD830) is used for the covering part at the tip of the finger and the plate-shaped part at the base. Both resins are oil resistant.

Kevlar thread is wound around the cylinder in a double helix at 2.5 mm intervals to prevent the cylinder from expanding in the radial direction. The outer shell and the cylinder are also constrained by Kevlar thread. Moreover, a cloth is glued or 0.5 mm thick vinyl chloride is screwed to the ventral side in order to reinforce the outer shell and suppress elongation in the length direction.

3. Development of soft robotic gripper actuated by oil pressure

3.1. Outline of oil-pressure actuation

Figure 7 shows the outline of the hydraulic actuation in the soft robot that we develop. A hydraulic pump charges oil to fiber-constraint fingers and generates high pressure in the inner space. The other side of the pump is connected to the oil-reservoir, which is a small tank to store oil.

It is possible to actuate multiple fingers by multiple pumps by extending this structure. In this study, we select the actuation of two fingers by a single pump because we

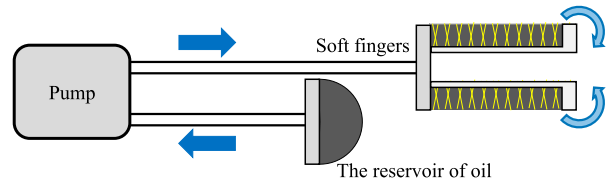


Figure 7. Outline of the hydraulic actuation.

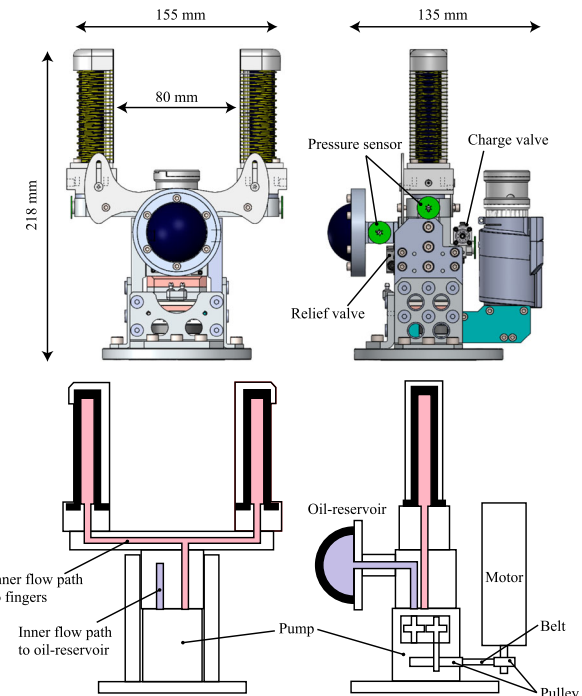


Figure 8. 3D CAD images of the developed soft robotic gripper and schematic illustrations of its inner structure.

focus on validating the soft robot structure and its performance. Also, a compact design is an important key factor for a real application. Therefore, we develop a gripper actuated by a single pump.

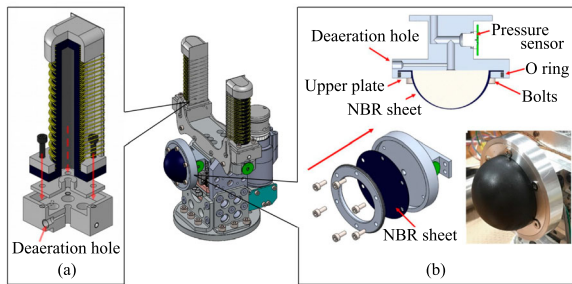


Figure 9. Structure of (a) the connecting parts of a finger and (b) the oil-reservoir. The base of the finger is sandwiched by a hard resin and a metal part to prevent the oil leakage. In the oil-reservoir, an NBR sheet is sandwiched between metal parts and sealed.

3.2. Design of miniaturized gripper

We developed a soft robotic gripper as shown in Figures 8–10. The upper row of Figure 8 shows 3D CAD images of the developed gripper. The total size is $218 \times 155 \times 135$ mm, and the weight is about 1.5 kg including the two soft fingers, oil-reservoir, pump, and electric motor. The distance between the fingers is 80 mm, assuming that the gripper holds daily-life objects. The lower row of Figure 8 shows schematic illustrations of the inner structure of the gripper. The pump is located close to the fingers, and they are connected through a pipeline inside duralumin parts. In the figure, the red line indicates the flow path from the pump to the fingers whereas the blue line indicates the flow path to the oil-reservoir. This design reduces the pipeline loss. This arrangement also contributes to compactness and ease of attachment of the gripper. Two pressure sensors are attached to measure the differential pressure generated by the pump.

Figure 9(a) shows the structure of the connecting parts of the finger. The base of the finger is sandwiched by a hard resin and a metal part to prevent the oil leakage. Figure 9(b) shows the oil-reservoir. A 0.5 mm thick NBR sheet is sandwiched by metal parts. After charging oil, it expands as shown in the figure. This half-sphere shape covers the amount of oil that flows into the two fingers during bending, and shrinks as the pump generates low pressure to the oil-reservoir and high pressure to the fingers. The external appearance of the gripper is shown in Figure 10. In situations such as those used in factories, finger covers are recommended to prevent contamination from oil leaks.

3.3. Hydraulic pump

We employ the small-size hydraulic pump developed by Komagata et al. [21]. This is an involute gear pump. The size is $47.2 \times 42 \times 32$ mm, and the weight is 216 g.

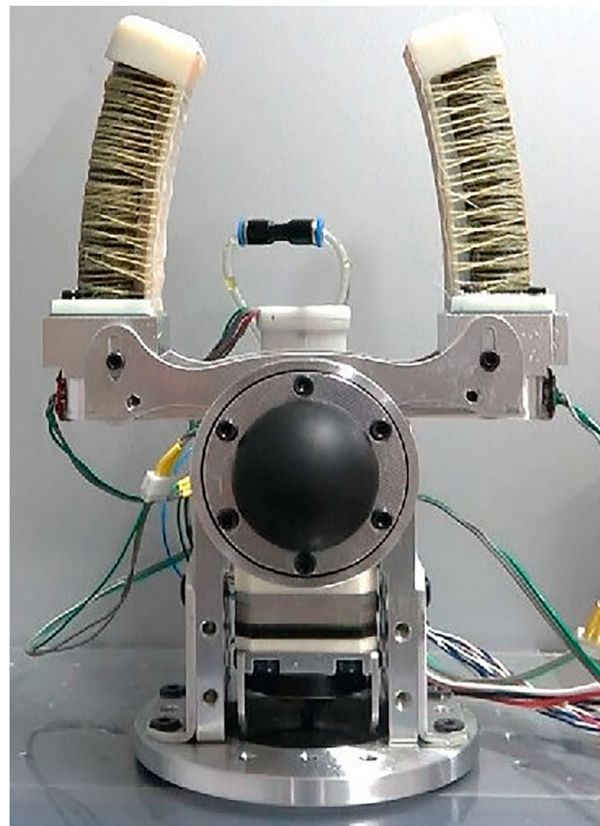


Figure 10. External appearance of the developed soft robotic gripper.

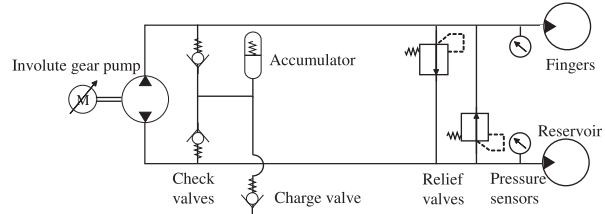


Figure 11. The closed hydraulic system of the soft robotic gripper.

The target discharge pressure of the small pump is originally 14 MPa and the discharge amount is 832 mm^3 . We assume that 3 MPa is enough to generate a bending motion of the fingers and redesigned the required torque of the pump and the reduction ratio between the motor and pump (see Appendix B for details).

Figure 11 shows the hydraulic system of the developed gripper. This is a closed hydraulic system. The function of each component is summarized as follows:

- The accumulator keeps the pressure to a certain level and also prevents the cavitation.
- The check valves open when the pressure becomes lower than a certain level, and let the flow of oil from

the accumulator to the hydraulic circuit. They are also opened to charge the oil into the circuit.

- The relief valve is a safety device to release excessive differential pressure.
- The charge valve is used for injecting oil from the outside in advance.

The number of parts is reduced compared to that in an open hydraulic system with control valves and large oil tank, downsizing the gripper.

4. Experimental validations of soft robotic gripper

4.1. Step response of pressure control

We report experimental validations of the developed gripper. First, we validate a basic performance of the pressure control of the pump. This control makes the differential pressure between the fingers and the reservoir close to a referential value. We employ the triple feedback control developed by Ko et al. [22] that consists of the pump pressure control, motor current control, and three-phase vector control.

Figure 12 shows the step response results of the pressure control with 1 MPa reference. In the figure, the blue dashed line indicates the referential value. We measured the responses in the case that two fingers were attached (indicated by the red line), and in the case that one finger was attached (indicated by the orange line) for a comparison. In the former, the time constant was 0.7 s assuming a first-order lag system. During this experiment, it took about 2 s until the fingers bent and touched each other, and until the fingers totally opened as well. In the case that one finger was attached, the other connector to a finger was closed. In this case, the time constant was 0.3 s.

As shown in Figure 12, there is a difference between the rise and the fall of the differential pressure. This is because the NBR part used in the oil-reservoir is thinner and more easily deformable than that used in the fingers, allowing oil to move quickly from the fingers to the reservoir.

4.2. Pressure–curvature relationship

Next, we evaluated the relationship between the curvature and pressure. In this paper, we assume (1) that the bending deformation of the finger is constrained on the frontal plane and (2) that the curvature is approximated to be constant, as shown in Figure 13.

Figure 14 shows the experimental setup. To obtain the curvature, we collected data of the position of the finger tip (marked by the red point in Figure 14) by

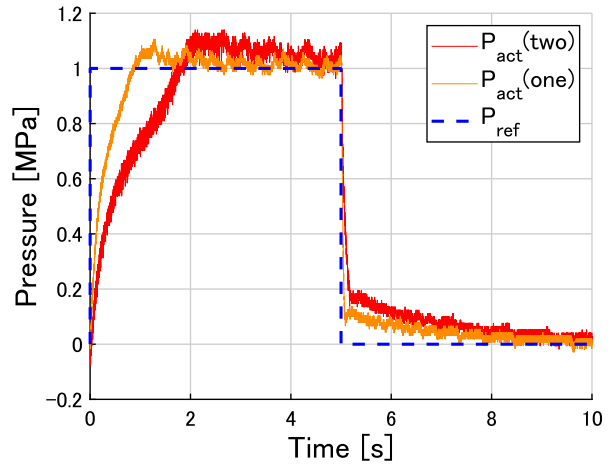


Figure 12. The blue line indicates reference pressure. The step response of the gripper with two fingers is the red line and the step response with only one finger is the orange line.

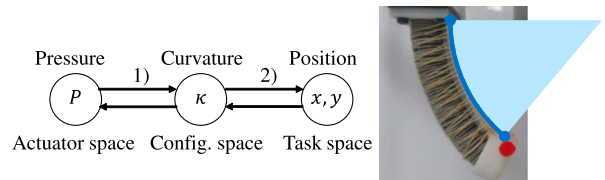


Figure 13. Mappings with constant curvature assumption: (1) robot specific and (2) robot independent.

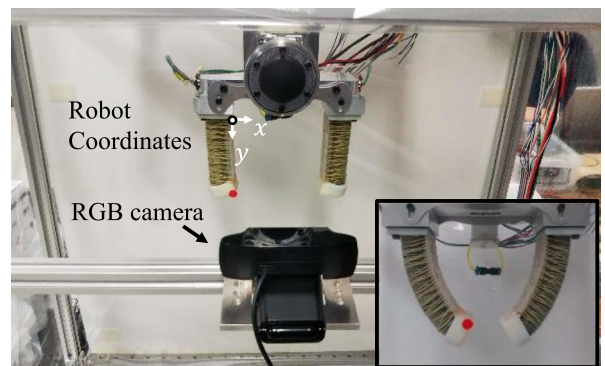


Figure 14. Camera setup for obtaining curvature data.

using an RGB camera. We use a perspective projection transformation without considering lens distortion (see Appendix C for details). From the constant curvature approximation, the curvature of the finger κ is calculated from the tip position x, y as follows:

$$\kappa = \frac{2x}{x^2 + y^2}. \quad (1)$$

Figure 15 shows the relationship between the pressure and curvature. We measured the relationship with two conditions of the pressure as follows:

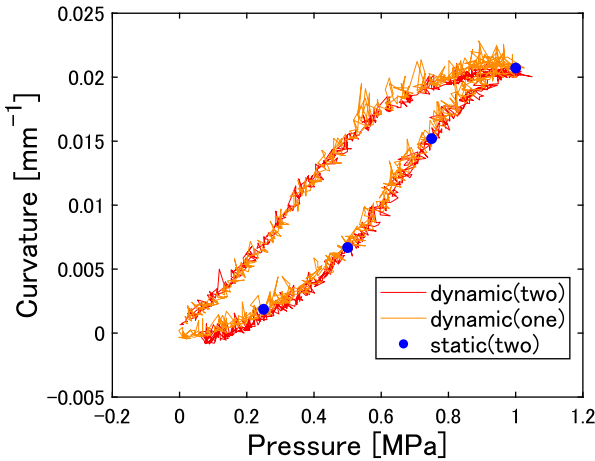


Figure 15. The blue dots indicate static response. The dynamic response of the gripper with two fingers is the red line and the dynamic response with only one finger is the orange line.

- *Static* condition (indicated by the blue dots) sets the reference to 0.25, 0.5, 0.75, and 1 MPa. For each reference value, we measured the curvature for 10 s and averaged the obtained data.
- *Dynamic* condition (indicated by the red line) sets the pressure reference as a ramp function to linearly increase from 0 to 1 MPa in 15 s, and then decrease in a similar manner. Figure 16 shows snapshots of the corresponding bending motion of the finger. As shown in Figure 15, a hysteresis is observed: the lower and upper paths are during expansion and contraction, respectively. When the oil is drained and the pressure descends, there is a delay in returning the expanded cylinder to its original state.

For a comparison, we also measured the dynamic condition with single finger (indicated by the orange line). The result of the response is similar to ones of the two fingers. When holding an object, only the expansion is included, therefore we ignore the contraction in later modeling.

4.3. Experiment of heavy object supporting

We tested an experiment of supporting a 5 kg load. Figure 17 shows the experimental view and the pressure

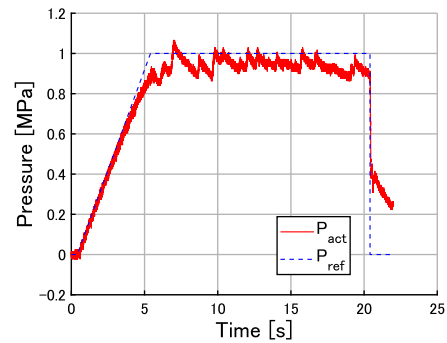
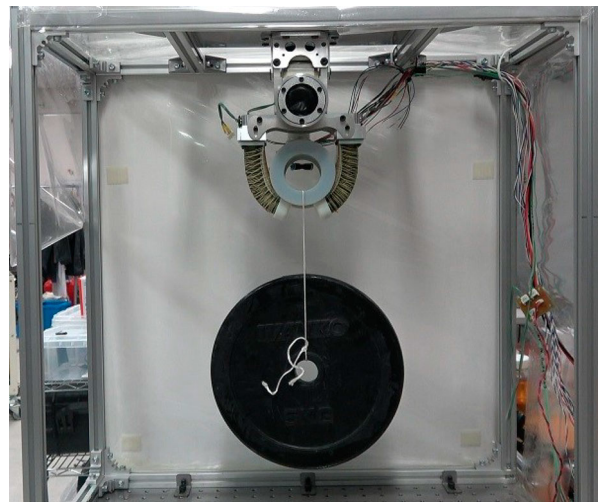


Figure 17. Supporting a 5 kg load with 1 MPa and the result of hydraulic pressure control while holding. The dashed blue line indicates the command value and the solid red line indicates the measured value.

response during the holding. This result shows that our gripper is capable of offering a larger payload capacity and supporting a much heavier object than tested in the literature.

Table 2 summarizes representative examples of soft robot hands that can support a heavy object. Our gripper is heavier because it contains a pump and a motor, and the width of the fingers is about the same as the others. Yap et al. [25] reported that their hand supported a 5 kg object by four fingers. Our gripper can support the 5 kg object by two fingers, which implies that each finger supports twice the load of the fingers in Yap et al.'s [25] paper. This result suggests that the oil-pressure actuation

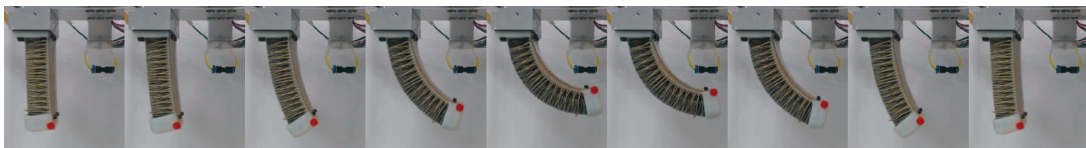


Figure 16. The snapshots of dynamic finger changes. $0 \text{ MPa} \rightarrow 0.25 \text{ MPa} \rightarrow 0.5 \text{ MPa} \rightarrow 0.75 \text{ MPa} \rightarrow 1 \text{ MPa} \rightarrow 0.75 \text{ MPa} \rightarrow 0.5 \text{ MPa} \rightarrow 0.25 \text{ MPa} \rightarrow 0 \text{ MPa}$.

Table 2. Soft robot hands that can support a heavy object.

	No. fingers	Width of a finger	Load	Weight
Dohta et al. [23]	four	12 or 15 mm	2.1 kg ^a	–
Zhou et al. [24]	two	25–50 mm	2.2 kg	200 g
Yap et al. [25]	four	25 mm	5 kg	277 g
Ours	two	26 mm	5 kg	1.5 kg

^a Dohta et al. [23] reported 20.8 N, and we converted it to kilogram-force.

extends the range of the application of soft robots to areas where human-scale payload capacity is required.

5. Application to visual-servo control

5.1. Curvature control by Bayes modeling and visual servo

In order to confirm the flexible bending to hold various objects, we performed holding experiments by visual servo.

In constant curvature assumption, the transformation connecting the pressure P and the curvature κ is robot-dependent, and the transformation connecting κ with the tip positions x and y is robot-independent (Equation (1)).

For robot-dependent transformations, Wang et al. [26] found the relationship by approximating the bending angle and extension length with a quadratic function of pressure. We also consider approximating the curvature with a quadratic function. Here, the data obtained in the finite element analysis are not always accurate in terms of material properties and the like. On the other hand, the data obtained in the experiment are measured using an external camera and the measurement error cannot be ignored. Therefore, we adopt the probabilistic method with Bayesian linear regression instead of definitive regression like the least squares method. A quadratic polynomial is used as the basis function. Then, the uncertainty of the data can be considered and overfitting can be suppressed. Furthermore, we can improve the accuracy of the model by updating the regression model with the data from the experiment after performing the regression with the data from the simulation. This is useful because collecting many data from an actual soft robot is not always easy. Specifically, we explain the pressure P and the curvature κ , which are N data sets. Assuming that the prior distribution of the regression weight parameter w is

$$p(w) = \mathcal{N}(w|\mathbf{0}, \alpha^{-1}\mathbf{I}) \quad (2)$$

and that the likelihood function is

$$p(\kappa|P, w) = \prod_{i=1}^N \mathcal{N}(\kappa_i | w^T \phi(P_i), \beta^{-1}) \quad (3)$$

from the data, the posterior distribution of the parameters is as follows. Here, α and β are hyperparameters

related to variance. M is the number of dimensions of the basis function $\phi(P_i)$, which is 3 in the quadratic polynomial.

$$p(w|P, \kappa) = \mathcal{N}(w|\mu_N, \Sigma_N) \quad (4a)$$

$$\mu_N = \beta \Sigma_N \Phi^T \kappa \quad (4b)$$

$$\Sigma_N^{-1} = \alpha \mathbf{I} + \beta \Phi^T \Phi \quad (4c)$$

$$\Phi = \begin{bmatrix} \phi_1(P_1) & \cdots & \phi_M(P_1) \\ \vdots & \ddots & \vdots \\ \phi_1(P_N) & \cdots & \phi_M(P_N) \end{bmatrix} \quad (4d)$$

When N' additional data are obtained, this posterior distribution can be updated as follows:

$$p(w|P', \kappa', P, \kappa) = \mathcal{N}(w|\mu_{N+N'}, \Sigma_{N+N'}) \quad (5a)$$

$$\mu_{N+N'} = \Sigma_{N+N'} (\Sigma_N^{-1} \mu_N + \beta \Phi'^T \kappa') \quad (5b)$$

$$\Sigma_{N+N'}^{-1} = \Sigma_N^{-1} + \beta \Phi'^T \Phi' \quad (5c)$$

$$\Phi' = \begin{bmatrix} \phi_1(P_{N+1}) & \cdots & \phi_M(P_{N+1}) \\ \vdots & \ddots & \vdots \\ \phi_1(P_{N+N'}) & \cdots & \phi_M(P_{N+N'}) \end{bmatrix} \quad (5d)$$

Then, by using the posterior distribution, the predicted distribution of the output κ for the new input P becomes as follows:

$$p(\kappa|P, P, \kappa) = \mathcal{N}(\kappa|\mu_N^T \phi(P), \beta^{-1} + \phi(P)^T \Sigma_N \phi(P)) \quad (6)$$

Therefore, when the obtained μ_N is adopted as the regression weight parameter w , a quadratic polynomial becomes as follows:

$$\kappa = w_2 P^2 + w_1 P + w_0 \quad (7)$$

The inverse transformation is as follows. The solution is uniquely determined because the relationship between pressure and curvature is monotonically increasing here

$$P = \frac{-w_1 + \sqrt{w_1^2 - 4w_2(w_0 - \kappa)}}{2w_2} \quad (8)$$

Furthermore, Jacobian can be obtained as follows:

$$\dot{\kappa} = J \dot{P} \quad J := 2w_2 P + w_1 \quad (9)$$

The thickness of NBR used here is 2 mm. First, we collected data from finite element analysis using Abaqus. The material properties are shown in Table 3. The properties of Kevlar thread and NBR are the same as those in Section 2. Properties of the cloth are the same as Kevlar thread and thickness is 0.1 mm. Young's modulus of resins is calculated from Shore A hardness using the

Table 3. The material properties of the soft finger for FEA simulation.

Material	Young's modulus (MPa)	Poisson's ratio
NBR	5.7	0.49
VeroWhite	1.46×10^3	0.49
TangoGray	7.1	0.49
Kevlar thread	31.067×10^3	0.36
Cloth	31.067×10^3	0.36

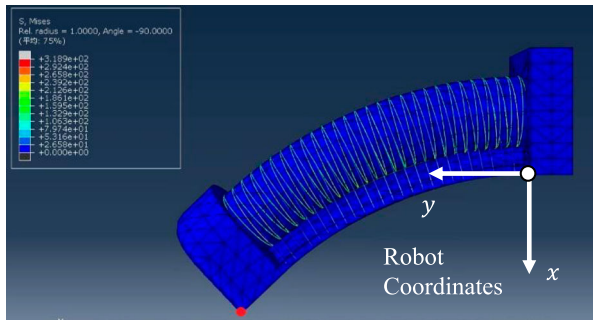


Figure 18. The FEA simulation result of a fiber constraint soft finger when pressurized at 0.5 MPa uniformly on the internal surface of the NBR cylinder.

following equation [27]:

$$H = 100\text{erf}(kE^{1/2}) \quad \text{where } k = 3.186 \times 10^{-4} \text{ Pa}^{-1/2} \quad (10)$$

Here, H is the shore hardness, E (MPa) is Young's modulus, and erf is an error function. Incompressibility is assumed for Poisson's ratio.

We applied pressure to the entire surface inside the cylinder, and collected data as shown in Figure 18.

Figure 19 shows the result of Bayesian linear regression from 42 data of the previous finite element analysis and the result updated using 100 data of the actual gripper. The pressure command was given by the ramp input and tip position data during which expansion was collected.

Visual servo is a method of controlling a robot by incorporating visual information obtained from a camera into a feedback loop [28, 29]. In soft robots, there is a method of controlling the tip position by attaching a marker to the tip and calculating the curvature [30]. We consider two-degree-of-freedom control that consists of a feedforward term and a feedback term as shown in Figure 20. The feedforward term is as follows. κ_{ref} is the target curvature in robot coordinates

$$P_{FF} = \frac{-w_1 + \sqrt{w_1^2 - 4w_2(w_0 - \kappa_{ref})}}{2w_2} \quad (11)$$

The feedback term is as follows. k_P is the feedback gain, usually 1.

$$P_{FB} = k_P J^{-1}(\kappa_{ref} - \kappa) \quad (12)$$

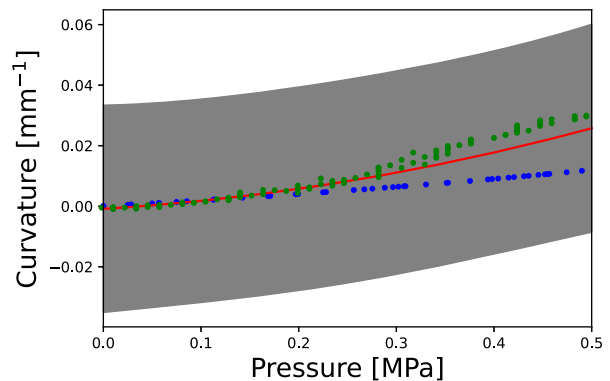


Figure 19. Results of Bayesian linear regression (the hyperparameter α is 0.01 and β is 900). First, we use only simulation results, and update the Bayes model with real data in the experiment. The blue points are data in simulation, the green points are data in the experiment, and the red line shows the regression curve using the average value of the weight parameters. In addition, the region of mean \pm standard deviation in the predicted distribution is colored gray. Here, $w_0 = -0.0008$, $w_1 = -0.0196$, $w_2 = -0.0673$.

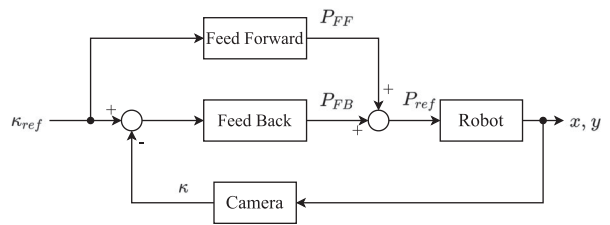


Figure 20. Two-degree-of-freedom curvature control.

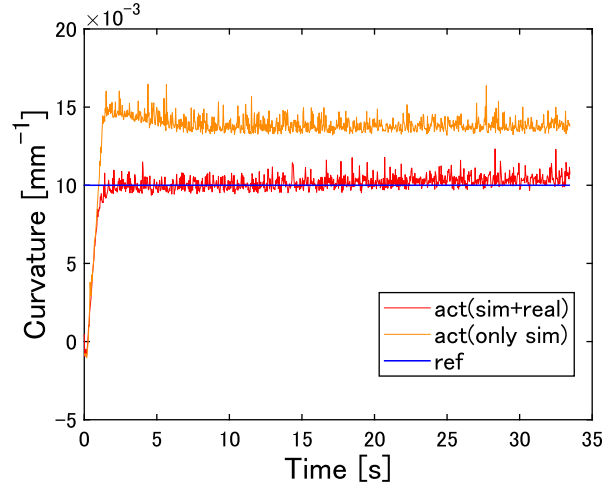


Figure 21. The blue line indicates reference curvature. After updating the Bayes model with real data (red), the error becomes smaller than before the update (orange).

It is considered that the vibration is suppressed by the viscosity of the rubber, therefore the differential term of the curvature error is not added. In control, $P_{ref} = P_{FF} + P_{FB}$ is set as the pressure command value.

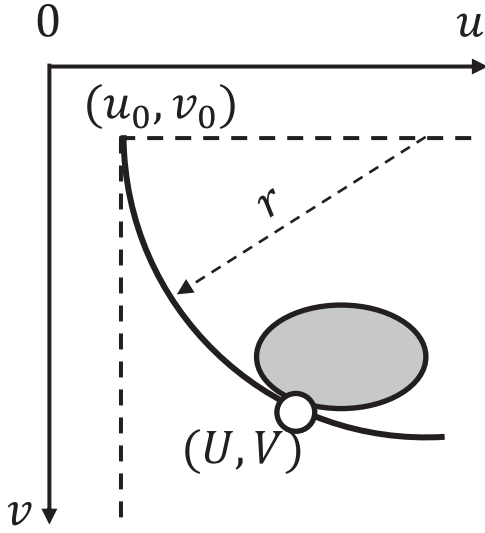


Figure 22. The relationship between a target position and arc in the image coordinates. (u_0, v_0) is the robot coordinates origin and (U, V) is the contact point.

We performed a follow-up experiment to a constant curvature with this control method. A red marker was attached to the tip of the finger and the position was determined by color detection after removing noise with a 5×5 median filter for the image. The μ_N obtained from Bayesian linear regression is adopted as the weight parameter w . The target curvature was set to 0.01 mm^{-1} , and the feedback gain was 1.0. The FPS of the camera was 30. the target curvature and the actual curvature are shown in Figure 21.

This visual servo was used to hold objects colored in green. The position of the object in image coordinates is obtained by color detection. As shown in Figure 22, the

Table 4. The number of images in data sets.

Domain	Train	Test	Used for
Source	171	20	Domain adaptation
Target	188	21	Both
Random	171	20	Domain randomization

radius r can be obtained from the positions of the object (u, v) in the image coordinates

$$\max_{u,v} r \text{ s.t. } (u - u_0)^2 + (v - v_0)^2 = r^2 \quad (13)$$

That is, we can get the contact point (U, V) as follows. This (U, V) can be converted to a position on the robot coordinates, and the target curvature can be calculated.

$$U, V = \arg \max_{u,v} \frac{(u - u_0)^2 + (v - v_0)^2}{2(u - u_0)} \quad (14)$$

The results are shown in Figure 23. The tracking error is thought to occur because the red marker cannot be brought closer depending on the contact state with the object, and static modeling is performed without considering the weight of the object. Because of its high stiffness, the function as a soft robot of absorbing excessive force due to the tracking error must be achieved by the softness of the material near the surface in contact with the object.

5.2. Target recognition by deep learning

We use domain adaptation or domain randomization [31] to determine the position of not only green objects but general objects such as daily necessities. First, we created data sets as shown in Figure 24 and Table 4.

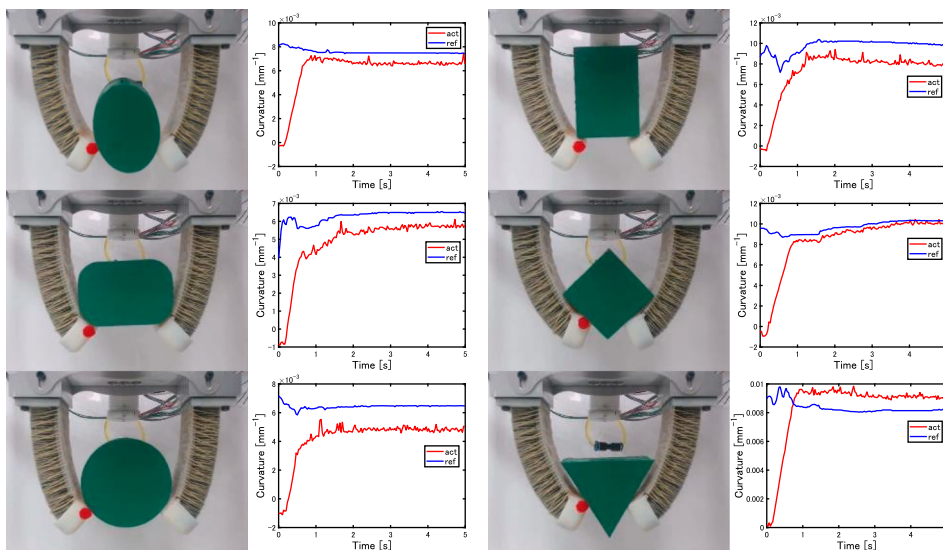
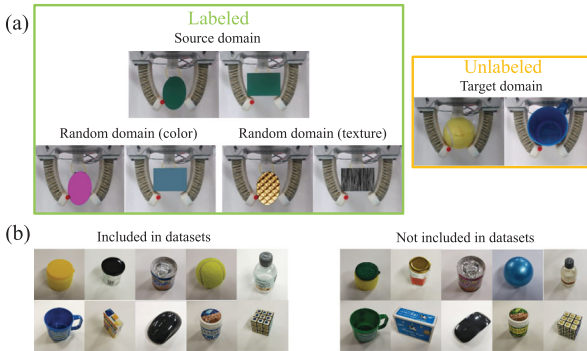


Figure 23. The change of curvature while holding green objects. The blue line indicates target curvature and the red line indicates actual curvature. The gripper holds six objects: ellipse, rectangle with rounded corners, cylinder, rectangle, square, and equilateral triangle.

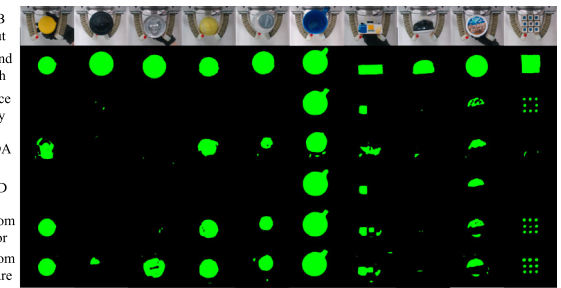
Table 5. Lightweight FCN model.

Layer	Output size
Input	$3 \times 480 \times 640$
Convolution + ReLU	$64 \times 240 \times 320$
Max Pooling	$64 \times 120 \times 160$
Convolution + ReLU	$128 \times 60 \times 80$
Max Pooling	$128 \times 30 \times 40$
Convolution + ReLU	$128 \times 30 \times 40$
Convolution + ReLU	$128 \times 30 \times 40$
Convolution	$128 \times 30 \times 40$
Deconvolution	$2 \times 480 \times 640$

**Figure 24.** (a) Examples of data sets and (b) daily necessities.

The data set of the green-colored object (source domain) is obtained by cutting out one image every 0.5 s from the videos of the previous experiments. There are six objects, and each has two orientations except for the cylinder. Therefore, there are a total of 12 types of movements, including holding nothing. The labels are created by green color detection. The data set of general objects (target domain) is also obtained from the video of holding 10 daily necessities. However, since the object cannot be detected before learning, a pressure command is manually given to bend fingers, and the object is placed on them to take a video. There was no label, but a label was manually created for the test image for evaluation. These data sets are used in two domain adaptation methods, ADDA [32] and MCD [33].

Furthermore, the randomized data set (referred to here as random domain) is created from the source domain data set. After the green color detection, the color or the texture of that part is randomly changed. In domain randomization, the deep learning model is

**Figure 25.** Qualitative results on daily necessities included in the target domain data set. The green areas indicate the objects detected by semantic segmentation.

trained using this data set, and performance is evaluated with the target domain.

A lightweight FCN [34] is used for the semantic segmentation to detect objects. The structure of the model is shown in Table 5. The input is an RGB image whose pixel value is expressed by a real number from 0 to 1. All methods were trained with a batch size of 8 and 500 epoch, and Adam [35] was used for optimization. Table 6 shows the results of quantitative evaluation for the test images of each domain.

Figure 25 shows some examples of the prediction results. Domain randomization about texture showed the best performance. Since the task has a small number of data sets, bridging the difference between source and target at the data set level is considered effective. The black and white parts included in objects could not be detected probably because the gloves and background were learned not to be classified as objects. As a countermeasure, it is conceivable to take a video with gloves or a background with some texture.

We performed holding experiments on objects in the target domain and another 10 objects not included in the data set. The position of the object is obtained by the model trained with domain randomization about texture. Other parts such as contact point calculation and curvature control are the same as in the previous subsection. The results are shown in Table 7. Figure 26 shows an example of successful holding. When the target object could not be detected, the target curvature suddenly changed or could not be calculated, and the object

Table 6. Evaluation of semantic segmentation for test data sets.

Method	Pixel accuracy			Mean IoU		
	Source	Random	Target	Source	Random	Target
Source only	99.86%	–	88.18%	98.56%	–	25.27%
ADDA	99.79%	–	87.91%	97.87%	–	29.70%
MCD	99.89%	–	87.96%	98.80%	–	23.63%
Random color	99.48%	99.28%	90.60%	94.80%	93.13%	43.00%
Random texture	99.54%	99.77%	92.45%	95.44%	97.77%	52.90%

Table 7. The result of success or failure of holding.

Objects	Glue	Bottle	Can	Ball	PET bottle	Cup	Box	Mouse	Gum	Rubik's cube
In data	\$✓\$	✗	✓	\$✓\$	△	\$✓\$	\$✓\$	✗	△	△
Not in data	\$✓\$	\$✓\$	✓	\$✓\$	△	\$✓\$	\$✓\$	✗	△	△

Note: The triangle mark is one that can be held although the image recognition is insufficient.

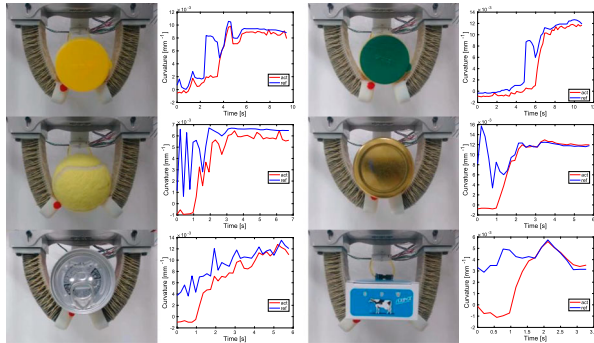


Figure 26. The examples of successful holding and the change of curvature. The blue line indicates target curvature and the red line indicates actual curvature.

dropped. When only a part of the target object such as a seal or lid was detected, fingers tracked the calculated target curvature which did not match the actual shape and bent until they touched each other. Therefore, as we mentioned earlier, the softness of the material near the surface in contact with the object is important. Also, if the object is asymmetrical, it is expected that holding will be stable with the fingers bent almost the same when pinched or grasped with some force. It is because the same pressure is applied to the fingers by one pump and the fingers try to carry the object toward the middle of them.

6. Conclusion

In this study, we developed the soft robotic gripper actuated by the oil-pressure and investigated the compatibility between the soft deformation and high stiffness. The obtained results are summarized as follows:

- (1) We analyzed the effect of the inner pressure, the fluid, and the fiber-constraint to the stiffness of the inflatable structure. The results of the finite element analysis of a simple inflatable shell structure revealed that the 1 MPa inner pressure with the fiber-constraint achieved 250 N/mm stiffness, which was comparable to the human muscle tendon, and that the incompressive fluid achieved higher stiffness than the compressive one.
- (2) We developed the soft robotic gripper consisting of the fiber-constraint fingers made with NBR and a self-contained oil pump. The time constant of the 1 MPa pressure control was 0.7 s, which implies that

the developed hand can achieve a moving speed sufficient for a human-scale function. Moreover, we showed that the developed hand could support a 5 kg object by two fingers.

- (3) The applications of the modeling and visual servo control methods were presented. The Bayes modeling method was able to consider uncertainties in the flexible bending motion, which improved the performance of the visual servo control of the finger curvature. Moreover, we demonstrated a variety of holding experiments combined with the object recognition by deep learning.

Notes

1. We examined the oil resistance of the rubber-like resin by immersing a test piece of about 2 g in oil for seven days. We confirmed that there was no change in mass in units of 0.1 g, in addition to the information released by the manufacturer companies.
2. The maximum tensile strength of rubber-like resin TangoGray (FLX950) is 3–5 MPa [19] while those of FKM, NBR, and ACM are 21, 28, and 17 MPa, respectively [20].

Disclosure statement

No potential conflict of interest was reported by the author(s).

Funding

This research was supported by JSPS Grants-in-Aid for Scientific Research (KAKENHI) under Grant Number JP19H05324.

Notes on contributors

Keisuke Hagiwara received his BEng and MEng degrees in Mechano-Informatics from the University of Tokyo in 2019 and 2021, respectively. His research interests include soft robotics, hydraulic actuators, and computer vision. He is a member of JSME.

Ko Yamamoto received the PhD degree in mechano-informatics from the University of Tokyo, Tokyo, Japan, in 2009. He is an Associate Professor with the Department of Mechano-informatics, University of Tokyo. He was a Postdoctoral Research Fellow with the Tokyo Institute of Technology in 2009–2012, and an Assistant Professor with Nagoya University in 2012–2014. He joined the University of Tokyo as an Assistant Professor in 2014, and was a Project Lecturer with the Department of Mechanical Engineering in 2016–2017. He was also a Visiting Researcher with Stanford University,

Stanford, CA, USA, in 2012. His research interests include mechanical design, dynamics computation and motion control of humanoid robots and soft robots, biomechanical analysis based on human musculo-skeletal model, and modeling and control of swarm robots and pedestrian crowds. Dr Yamamoto is a Member of the Japan Society of Mechanical Engineers, the Robotics Society of Japan and IEEE.

Yoshihisa Shibata received his BEng and MEng degrees in Mechano-Informatics from the University of Tokyo in 2018 and 2020, respectively. He was Project Academic Support Staff at the University of Tokyo from 2020 to 2021. His research interests include soft robotics and hydraulic actuators. He is a member of JSME.

Mitsuo Komagata is Project Assistant Professor, Department of Mechano-informatics, University of Tokyo. He received his BEng, MEng, and PhD degrees in Mechano-Informatics from the University of Tokyo in 2014, 2016, and 2020, respectively. He was Project Researcher at the University of Tokyo (2020). His research interests include actuations and mechanical design. He is a member of IEEE and RSJ.

Yoshihiko Nakamura is Senior Researcher with Corporate Sponsored Research Program 'Human Motion Data Science', Research into Artifacts Center for Engineering, Graduate School of Engineering, University of Tokyo. He received PhD in 1985 from Kyoto University and held faculty positions in Kyoto University, University of California Santa Barbara and University of Tokyo. His fields of research started from redundancy of robot manipulators and kinodynamics of large DOF robot systems, and include humanoid robotics, cognitive robotics, neuro-musculoskeletal human model, and their computational algorithms. He is a recipient of King-Sun Fu Memorial Best Transactions Paper Award, IEEE Transaction of Robotics and Automation in 2001 and 2002, JSME Medal for Distinguished Engineers in 2019, Pioneer Award of IEEE-RAS in 2021, and Tateisi Prize Achievement Award in 2022. Dr Nakamura is Foreign Member of Academy of Engineering Science of Serbia, TUM Distinguished Affiliated Professor of Technische Universität München, Fellow of JSME, RSJ, and World Academy of Art and Science, Life Fellow of IEEE, and Professor Emeritus of University of Tokyo.

ORCID

- Keisuke Hagiwara  <http://orcid.org/0000-0002-2869-3289>
 Ko Yamamoto  <http://orcid.org/0000-0002-9558-3880>
 Yoshihisa Shibata  <http://orcid.org/0000-0002-5221-2772>
 Mitsuo Komagata  <http://orcid.org/0000-0001-8884-2023>
 Yoshihiko Nakamura  <http://orcid.org/0000-0001-7162-5102>

References

- [1] Wikipedia. Cobot ; 2022. Available from: <https://en.wikipedia.org/wiki/Cobot>.
- [2] Rus D, Tolley MT. Design, fabrication and control of soft robots. *Nature*. 2015;521(7553):467–475.
- [3] Pfeifer R, Lungarella M, Iida F. The challenges ahead for bio-inspired soft robotics. *Commun ACM*. 2012;55(11):76–87.
- [4] Ansari Y, Hassan T, Manti M, et al. Soft robotic technologies for industrial applications. *Proceedings of the European Projects in Knowledge Applications and Intelligent Systems*; Lisbon: 2016. p. 35–64.
- [5] Cianchetti M, Ranzani T, Gerboni G, et al. Soft robotics technologies to address shortcomings in today's minimally invasive surgery: the stiff-flop approach. *Soft Robot*. 2014;1(2):122–131.
- [6] Peng Z, Huang J. Soft rehabilitation and nursing-care robots: A review and future outlook. *Appl Sci*. 2019;9(15):3102.
- [7] Takeichi M, Suzumori K, Endo G, et al. Development of Giacometti arm with balloon body. *IEEE Robot Autom Lett*. 2017;2(2):951–957.
- [8] Wang Z, Torigoe Y, Hirai S. A prestressed soft gripper: design, modeling, fabrication, and tests for food handling. *IEEE Robot Autom Lett*. 2017;2(4):1909–1916.
- [9] Soft Robotics Inc. mgrip ; 2021. Available from: <https://www.softroboticsinc.com/products/mgrip>.
- [10] Morita R, Nabae H, Endo G, et al. A proposal of a new rotational-compliant joint with oil-hydraulic McKibben artificial muscles. *Adv Robot*. 2018;32(9):511–523.
- [11] Shintake J, Cacucciolo V, Floreano D, et al. Soft robotic grippers. *Adv Mater*. 2018;30(29): Article Id 1707035.
- [12] Udupa G, Sreedharan P, Aditya K. Robotic gripper driven by flexible microactuator based on an innovative technique. *Proceedings of the IEEE Workshop on Advanced Robotics and its Social Impacts (ARSO'10)*; Seoul: 2010. p. 111–116.
- [13] Zhang H, Kumar AS, Chen F, et al. Topology optimized multimaterial soft fingers for applications on grippers, rehabilitation, and artificial hands. *IEEE ASME Trans Mechatron*. 2018;24(1):120–131.
- [14] Katzschatzmann RK, Marchese AD, Rus D. Autonomous object manipulation using a soft planar grasping manipulator. *Soft Robot*. 2015;2(4):155–164.
- [15] Suzumori K, Iikura S, Tanaka H. Applying a flexible microactuator to robotic mechanisms. *IEEE Control Syst Mag*. 1992;12(1):21–27.
- [16] Deimel R, Brock O. A novel type of compliant and underactuated robotic hand for dexterous grasping. *Int J Rob Res*. 2016;35(1–3):161–185.
- [17] Gent AN. Rubber and rubber elasticity: a review. *J Polym Sci: Polym Symp*. 1974;48(1):1–17.
- [18] Cook CS, McDonagh MJN. Measurement of muscle and tendon stiffness in man. *Eur J Appl Physiol Occup Physiol*. 1996;72(4):380–382.
- [19] Stratasys Ltd. Tango polyjet simulated rubber material ; 2021. Available from: https://www.stratasys.com/-/media/files/material-spec-sheets/mss_pj_tango_0318a.pdf.
- [20] Schaefer RJ. Mechanical properties of rubber. In: Piersol A, Paez T, editors. *Harris' shock and vibration handbook*. 6th ed. New York (NY): McGraw-Hill Companies Inc; 2010. p. 33.1–33.18.
- [21] Komagata M, Ko T, Nakamura Y. Design and development of compact ceramics reinforced pump with low internal leakage for electro-hydrostatic actuated robots. *Proceedings of the IFTOMM World Congress (IFTOMM'19)*; Krakow: 2019. p. 2439–2448.
- [22] Ko T, Kaminaga H, Nakamura Y. Current-pressure-position triple-loop feedback control of electro-hydrostatic

- actuators for humanoid robots. *Adv Robot.* **2018**;32(24):1269–1284.
- [23] Dohta S, Shinohara T, Matsushita H. Development of a pneumatic rubber hand. Proceedings of the JFPS International Symposium on Fluid Power; Nara: 2002. p. 49–54; 5–1.
- [24] Zhou J, Chen X, Li J, et al. A soft robotic approach to robust and dexterous grasping. Proceedings of the IEEE International Conference on Soft Robotics (RoboSoft'18); Livorno: 2018. p. 412–417.
- [25] Yap HK, Ng HY, Yeow C. High-force soft printable pneumatics for soft robotic applications. *Soft Robot.* **2016**;3(3):144–158.
- [26] Wang Y, Xu Q. Design and fabrication of a new dual-arm soft robotic manipulator. *Actuators.* **2019**;8(1):5.
- [27] Meththananda IM, Parker S, Patel MP, et al. The relationship between shore hardness of elastomeric dental materials and young's modulus. *Dent Mater.* **2009**;25(8):956–959.
- [28] Hutchinson S, Hager GD, Corke PI. A tutorial on visual servo control. *IEEE Trans Rob Autom.* **1996**;12(5):651–670.
- [29] Hutchinson S, Chaumette F. Visual servo control, part i: basic approaches. *IEEE Robot Autom Mag.* **2006**;13(4):82–90.
- [30] Chikhaoui MT, Cot A, Rabenorosoa K, et al. Design and closed-loop control of a tri-layer polypyrrole based telescopic soft robot. Proceedings of the IEEE/RSJ International Conference on Intelligent Robots and Systems (IROS'16); Daejeon: 2016. p. 1145–1150.
- [31] Tobin J, Fong R, Ray A, et al. Domain randomization for transferring deep neural networks from simulation to the real world. Proceedings of the IEEE/RSJ International Conference on Intelligent Robots and Systems (IROS'17); Vancouver: 2017. p. 23–30.
- [32] Tzeng E, Hoffman J, Saenko K, et al. Adversarial discriminative domain adaptation. Proceedings of the IEEE/RSJ Conference on Computer Vision and Pattern Recognition (CVPR'17); Honolulu (HI): 2017. p. 7167–7176.
- [33] Saito K, Watanabe K, Ushiku Y, et al. Maximum classifier discrepancy for unsupervised domain adaptation. Proceedings of the IEEE/RSJ Conference on Computer Vision and Pattern Recognition (CVPR'18); Salt Lake City (UT): 2018. p. 3723–3732.
- [34] Long J, Shelhamer E, Darrell T. Fully convolutional networks for semantic segmentation. Proceedings of the IEEE/RSJ Conference on Computer Vision and Pattern Recognition (CVPR'15); Boston (MA): 2015. p. 3431–3440.
- [35] Kingma DP, Ba J. Adam: a method for stochastic optimization. Proceedings of the IEEE/RSJ International Conference on Learning Representations (ICLR'15); San Diego (CA): 2015. p. 1–15.
- [36] Connolly F, Polygerinos P, Walsh CJ, et al. Mechanical programming of soft actuators by varying fiber angle. *Soft Robot.* **2015**;2(1):26–32.
- [37] The Society of Rubber Science and Technology, Japan. Rubber test method. 3rd ed. Tokyo, Japan: Maruzen Publishing; 2006. p. 203.
- [38] Zhang Z. A flexible new technique for camera calibration. *IEEE Trans Pattern Anal Mach Intell.* **2000**;22(11):1330–1334.

Appendix A. Parameter settings in FEA simulation of Section 2.2

Properties of Kevlar thread for fiber-constraint are based on Connolly et al. [36]. We calculate Young's modulus of NBR assuming hardness 70 using the following equation [37]:

$$H_A = \frac{\frac{8}{3}aH_0E - P_0}{\frac{8}{3}aH_0E + P_{100} - P_0} \times 100 \quad (\text{A1})$$

Here, H_A represents JIS HA hardness. The radius of the push needle a is 0.51 mm, the height of the push needle H_0 is 2.5 mm, the load P_0 is 0.55 N when the hardness is 0, and the load P_{100} is 8.05 N when the hardness is 100, respectively. Incompressibility is assumed for Poisson's ratio.

The bulk modulus of the oil is assumed to be 2 GPa. The air is treated as an ideal gas.

Appendix B. Required torque to drive hydraulic pump

The pump output W_p [W] and the shaft input W_a [W] are connected using the efficiency η .

$$W_p = \eta W_a \quad (\text{B1})$$

The pump output can be obtained from the differential pressure P [Pa] and the discharge amount per minute Q [m^3/min], and the shaft input can be obtained from the shaft torque T [$\text{N} \cdot \text{m}$] and the revolution speed N [rpm].

$$W_p = \frac{PQ}{60} \quad (\text{B2})$$

$$W_a = \frac{2\pi TN}{60} \quad (\text{B3})$$

The discharge amount can be obtained from the theoretical discharge amount per one rotation q [m^3/rev] and N by the following equation under the assumption of an ideal state with no internal leakage,

$$Q = qN = 2\pi m^2 z b N \quad (\text{B4})$$

where m [m] is the module, z [-] is the number of teeth of the pump's gear, and b [m] is the tooth width. Therefore, the required torque for the pump is calculated by this.

$$T = \eta^{-1} P m^2 z b \quad (\text{B5})$$

Assuming an efficiency η of 0.4 and a target pressure of 3 MPa, the torque required to drive the pump is 0.80 N · m from the parameters of the pump. The motor was decided to be a maxon motor AG's EC 4Pole 30 of 200 W, which is a small and high torque motor. The motor is assumed to be used at 10 A and its torque constant is 27.6 mN · m/A, therefore the motor torque is 0.276 N · m, and the reduction ratio should be 0.345 or less. Here, the rotation of the motor is transmitted to the pump by a timing belt. As a result, the reduction ratio was set to 0.3 by using pulleys with 12 and 40 teeth and a timing belt. Furthermore, the motor is covered with a water cooling jacket, thereby extending the continuous operation time.

Appendix C. Perspective projection transformation of RGB camera

Perspective projection transformation without considering lens distortion is represented as follows:

$$s \begin{bmatrix} u \\ v \\ 1 \end{bmatrix} = \mathbf{K}[\mathbf{R}|\mathbf{t}] \begin{bmatrix} x \\ y \\ z \\ 1 \end{bmatrix} \quad (\text{C1})$$

Here, u and v are the position in image coordinates, and x, y, z are the position in robot coordinates. $\mathbf{R} \in SO(3)$ and $\mathbf{t} \in \mathbb{R}^3$

are the rotation matrix and translation vector of the camera coordinates with respect to the robot coordinates, obtained by measuring after fixing the camera and the robot. $\mathbf{K} \in \mathbb{R}^{3 \times 3}$ is the internal parameter matrix of the camera, obtained by the calibration using a checkerboard [38]. s is a scalar. The tip position of soft finger in robot coordinates is calculated by $\mathbf{A}^\dagger \mathbf{m}$ from the tip position vector \mathbf{m} on the image coordinates. Here, $\mathbf{A} = s^{-1} \mathbf{K}[\mathbf{R}|\mathbf{t}]$, and \mathbf{A}^\dagger represents the pseudo-inverse matrix of \mathbf{A} .